We are IntechOpen, the world's leading publisher of Open Access books
Built by scientists, for scientists

6,900
Open access books available

185,000
International authors and editors

200M
Downloads

154
Countries delivered to

Our authors are among the

TOP 1%
most cited scientists

12.2%
Contributors from top 500 universities

CLARIVATE ANALYTICS

BOOK CITATION INDEX

INDEXED

WEB OF SCIENCE™

Selection of our books indexed in the Book Citation Index
in Web of Science™ Core Collection (BKCI)

Interested in publishing with us?
Contact book.department@intechopen.com

Point Diffraction Interferometry

Daodang Wang and Rongguang Liang

Additional information is available at the end of the chapter

Abstract

The point diffraction interferometer (PDI) employs a point-diffraction spherical wavefront as ideal measurement reference, and it overcomes the accuracy limitation of reference optics in traditional interferometers. To overcome the limitation of measurement range either with pinhole (low light transmission) or with single-mode fiber (low NA), a single-mode fiber with narrowed exit aperture has been proposed to obtain the point-diffraction wavefront with both high NA and high power. It is a key issue to analyze the point-diffraction wavefront error in PDI, which determines the achievable accuracy of the system. The FDTD method based on the vector diffraction theory provides a powerful tool for the design and optimization of the PDI system. In addition, a high-precision method based on shearing interferometry can be applied to measure point-diffraction wavefront with high NA, in which a double-step calibration including three-dimensional coordinate reconstruction and symmetric lateral displacement compensation is used to calibrate the geometric aberration. The PDI is expected to be a powerful tool for high-precision optical testing. With the PDI method, a high accuracy with RMS value better than subnanometer can be obtained in the optical surface testing and submicron in the absolute three-dimensional coordinate measurement, demonstrating the feasibility and wide application foreground of PDI.

Keywords: point diffraction, optical testing, pinhole, optical fiber, wavefront sphericity

1. Introduction

The development of optical design and fabrication such as projection optics for extreme ultraviolet lithography (EUVL) and laser fusion, etc. places ultrahigh requirement on the optical testing precision and accuracy. In the EUVL operating at a wavelength of 13.5 nm [1–4], the projection optics is composed of 4–6 aspheric mirrors and each mirror needs to be

finished with the figure error less than 0.2–0.3 nm (RMS), requiring a higher testing accuracy (e.g., 0.1 nm RMS). The optical interferometers, including the Twyman-Green [5] and Fizeau interferometers [6], have been widely used in the testing lenses and mirrors for figure metrology, in which standard lenses are applied to produce the necessary reference wavefront. Due to the fabricating error of the reference optics, the achievable measurement accuracy of the traditional interferometers is generally limited within $\lambda/50$ (λ is the operating wavelength). As a novel optical technique, the point-diffraction interferometer (PDI) [7–12] has been developed to overcome the accuracy limitation in traditional interferometers, and it can reach the measurement accuracy in the order of subnanometer. The PDI method employs point-diffraction spherical wavefront as ideal measurement reference, and it can achieve the accuracy better than $10^{-3}\lambda$. The PDI does not require precise and costly standard parts, and it provides a feasible way to overcome the accuracy limitation of the reference optics in traditional interferometers. The process of point diffraction determines the reachable accuracy of PDI, thus, a good reproducibility of the measurement accuracy can be achieved with PDI. The ideal spherical wave can be generated from the point-diffraction source such as circle pinhole [13–15] and optical fiber [16–18]. Nikon realized that the high-precision testing of spherical and aspherical surfaces with the pinhole PDI [14, 15], and the Lawrence Livermore National Laboratory measured surface figure with the single-mode-fiber PDI [16]. The diffracted wave in both PDI systems serves as testing wave as well as reference wave. To extend the aperture of the optics, a fiber PDI with two optical fibers serving as point sources was proposed for large optics measurement [18], in which the diffracted wave from one fiber acts as testing wave and that from the other fiber as reference wave. Considering the fact that the diffraction light power from pinhole is poor (transmittance <0.1‰) and the numerical aperture (NA) of diffracted wavefront with single-mode fiber is quite low (<0.20), both approaches limit the measurement range of the existing PDIs. A submicron-aperture (SMA) fiber with cone-shaped exit end has been proposed to obtain both the high diffraction light power and high-NA spherical wavefront [19–21], and it is considered as a feasible way to extend the measurement range of the system. Due to the fact that the achievable testing accuracy of PDI is mainly determined by the sphericity of diffracted wavefront, the analysis of the diffracted wavefront error has become a fundamental way to evaluate the performance of PDI. In our research, both numerical analysis and experimental measurement have been performed to reconstruct the point-diffraction wavefront aberration. Besides, various setups of PDI have been developed to realize the precise surface testing with adjustable contrast [12, 22] and three-dimensional (3D) coordinate measurement [20, 23, 24]. The new PDI for three-dimensional (3D) coordinate measurement avoids the measurement uncertainty introduced by the imperfect target in multilateration and allows the target (made of two point-diffraction sources) to take free movement within a volumetric space over NA of point-diffraction wave. Section 2 presents a brief review of the PDI for testing of wavefront and the optical surface. Section 3 presents the basic theory of the SMA fiber PDI for 3D coordinate measurement. Sections 4 and 5 explain the numerical method and the experimental measurement method for the evaluation of diffracted wavefront sphericity, as well as the corresponding analyzing results.

2. PDI for wavefront and surface testing

2.1. Wavefront testing with PDI

The PDI was first proposed by Smartt and Strong in 1972 [7]. The early version of the PDI was an interferometer using a PDI plate with partial transmission. **Figure 1** shows the principle of the PDI with partially transparent PDI plate. The PDI plate consists of an absorbing metal coating mask on a clear substrate and a tiny pinhole placed near focus to divide the wave into two parts, namely the testing wave and reference wave. The pinhole picks off part of the incident focused light wave and generates the diffracted spherical wavefront as reference wavefront. The test wave passes through the PDI plate and then interferes with diffracted spherical wave. The PDI can be used to measure the wavefront error from imaging optics and flow field, etc. In the design of the PDI shown in **Figure 1**, it is a key issue to determine the pinhole size and plate transmittance [9]. Due to the reduction in light intensity incident on the tiny pinhole, the controllable reduction in the test wave intensity by mask attenuation is required to get maximum fringe contrast.

Another PDI plate with double apertures has been applied in the PDI for the evaluation of wavefront error in imaging optics [25], as shown in **Figure 2**. A beam splitter such as the
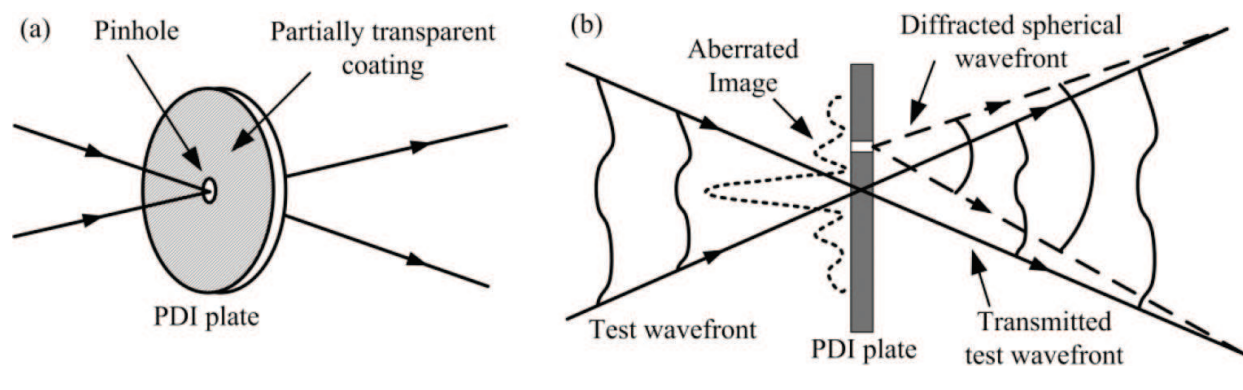

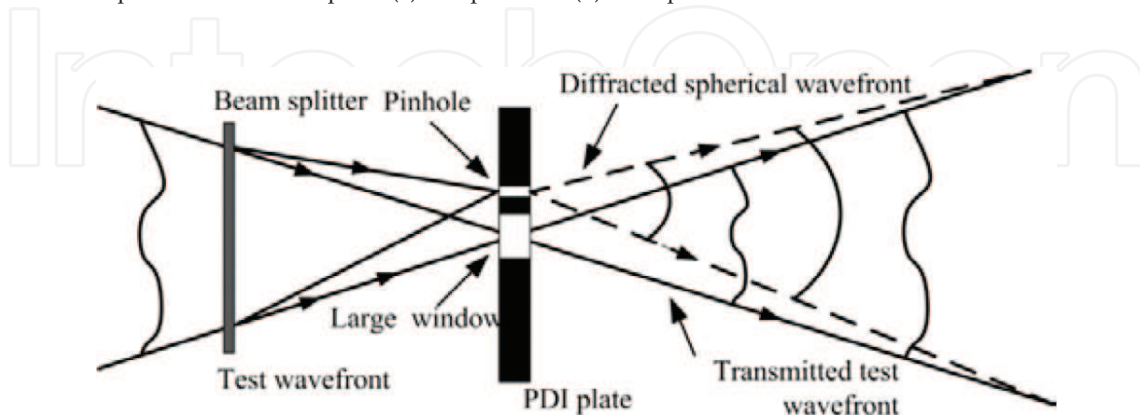**Figure 1.** Principle of PDI with PDI plate. (a) PDI plate and (b) PDI operation.

Figure 2. PDI plate with double aperture.

transmission grating is used to divide the test wave into two waves with a small angular separation. The PDI plate consists of one tiny pinhole and one large window on an opaque mask, and both of them are placed at the respect focal points of two beams. The pinhole is applied to generate the spherical reference wavefront by diffraction and the window transmits the test wave. The intensity of the diffracted wave relative to that of the conventional PDI is increased by several orders of magnitude. With the application of double-aperture PDI plate, there is no need to further attenuation in the test wave to match the intensities of interfering waves. Besides, the beam division enables the potential to introduce the various phase shifts between the interfering waves.

2.2. Optical surface testing with PDI

Figure 3 shows the typical configuration of PDI for optical surface testing. Either the pinhole (**Figure 3a**) [13–15] or the single-mode optical fiber (**Figure 3b**) [16–18] can be used as the point-diffraction source to generate the required spherical wavefront. The diffracted wavefront is separated to two parts, i.e., the test and reference wavefronts. The test wave travels toward the spherical surface under test, and the pinhole (exit end of fiber) is positioned at the curvature center of the test surface, so that the reflected wave from the test surface converges at the pinhole mirror (semitransparent metallic film on the output end of fiber) and then is reflected at the pinhole mirror (semitransparent metallic film on the output end of fiber). The test wave combines and interferes with the reference wave after reflection. By translating the test surface with a precise PZT scanner, the test surface error can be measured with the phase-shifting method. The selection of beam polarization state in the system can significantly influence the measurement. The polarization would affect the sphericity of the diffracted wavefront, and the reflection at mirror over a high NA can also introduce polarization-dependent phase shifts. In the PDI system, the polarization state of diffracted spherical wave is generally adjusted to be circularly polarized [26], in which the effect of polarization on the measurement precision is negligible.
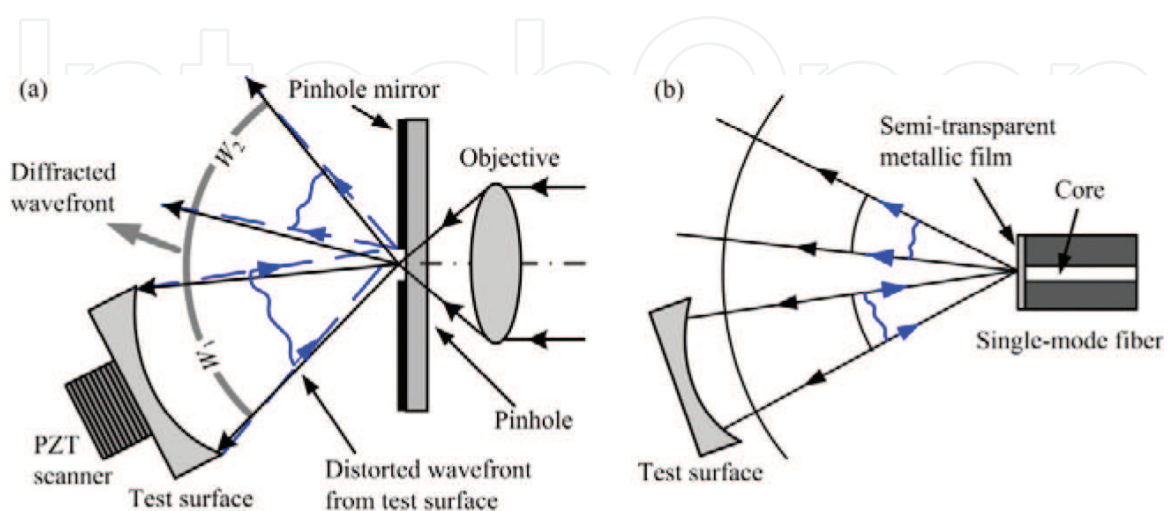

Figure 3. Configuration of PDI for optical surface testing. (a) Pinhole PDI [13], (b) single-mode fiber PDI [16].

In the PDI with pinhole method, the circular pinhole of submicron (or even smaller) diameter is adopted to obtain high measurable NA. **Figure 4(a)** shows a scanning-electron microscope (SEM) picture of the pinhole fabricated by etching the chromium film with the focused ion-beam etching (FIBE) method [22], in which the metallic layer is sputtered onto the silica substrate. A nearly perfect circular pinhole can be obtained with the FIBE method. The high measurable NA can be achieved with the pinhole method; however, the nonadjustable fringe contrast would limit the measurement accuracy in the testing of low-reflectivity surface, due to the poor fringe contrast and difficulty in fringe processing.

A pinhole PDI with adjustable fringe contrast can be adopted for the testing of high-NA spherical surfaces with low reflectivity [22]. The polarizing elements are applied to transform
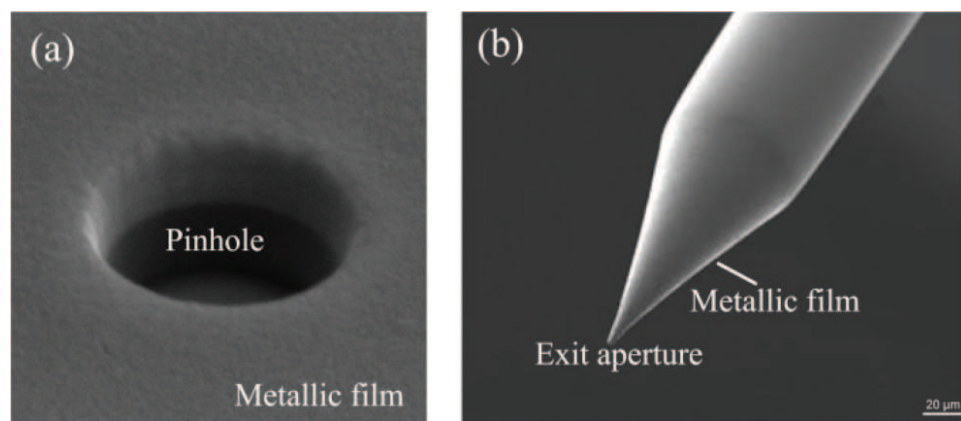

Figure 4. Point diffraction sources in PDI. (a) Pinhole [22], and (b) submicron-aperture fiber [21].
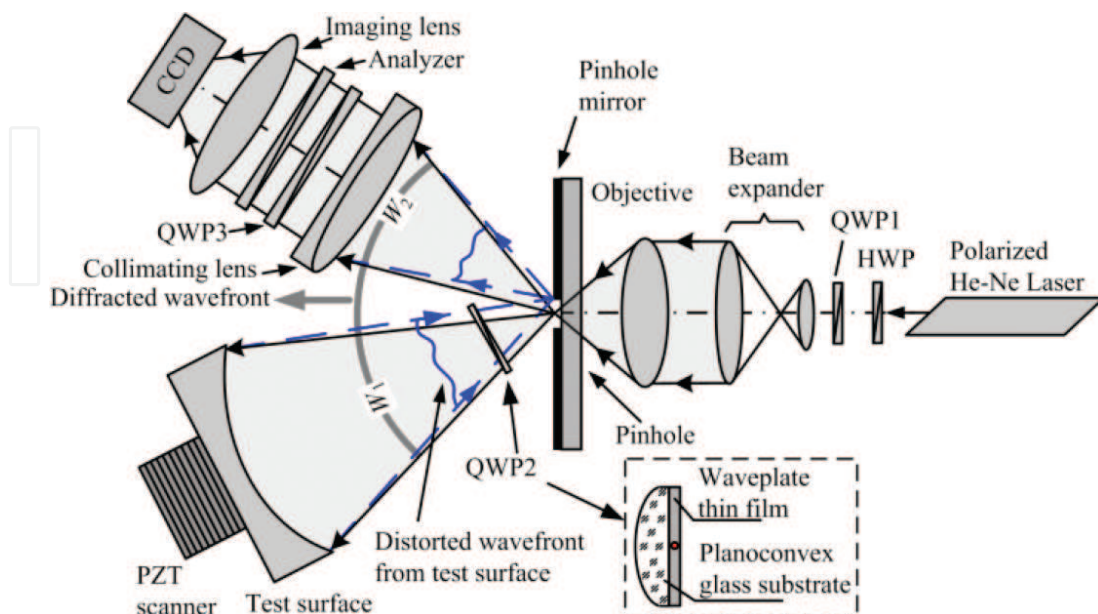

Figure 5. Configuration of pinhole PDI with adjustable fringe contrast [22].

the polarization states and adjust the relative intensities of the interfering beams, by which the adjustable fringe contrast can be achieved. **Figure 5** shows the optical configuration of the pinhole PDI with adjustable fringe contrast. A quarter-wave plate (QWP2) with special structure (consisting of a thin waveplate film and a plano-convex substrate) is placed at the test path, with the fast axis oriented at −45° to horizontal. The diffracted wave is adjusted to be circularly polarized. The test wave W_1 travels toward the test surface and passes through QWP2 twice, respectively, before and after the reflection at the test surface, then the test wave W_1 becomes opposite circularly polarized with respect to the reference wave W_2. The relative intensities of the test and reference beams can be adjusted by rotating the transmission axis of the analyzer, realizing the adjustable fringe contrast. Due to the fact that the diffracted wave is divergent, QWP2 in the test path would introduce different phase retardations in various directions. To minimize the effect of QWP2 on the divergent test wave, a true zero-order waveplate, which has advantages of less sensitive to variation in angle of incidence and wavelength, is employed in the system. In the true zero-order waveplate, a thin waveplate film is cemented on the glass substrate. To minimize the aberrations introduced by the glass substrate in the case of divergent waves, a plano-convex substrate is used in the true zero-order waveplate QWP2.

Figure 6 shows the testing results about a spherical surface with the reflectivity 4%, NA 0.40 and aperture diameter 137.7 mm. **Figure 6(a)** is the surface error measured with the adjustable-contrast pinhole PDI system shown in **Figure 5**, and **Figure 6(b)** is that obtained with the ZYGO interferometer. According to **Figure 6**, a good agreement between the PDI result and that from the ZYGO interferometer is achieved, and the PV and RMS differences between the testing results are about 0.0214λ and 0.0025λ, respectively. Thus, high-accuracy testing of the surface with low reflectivity is realized with the adjustable-contrast PDI system.

The light transmission through the pinhole is quite low (<0.1‰), and it significantly limits the achievable measurement range of the pinhole PDI. In the PDI with single-mode fiber, the
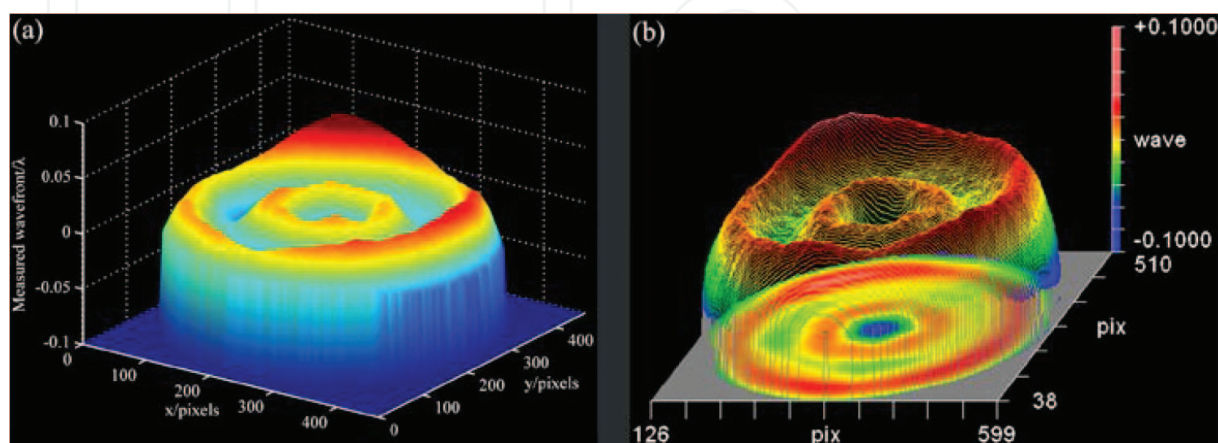

Figure 6. Measured surface error of test spherical surface with (a) the adjustable-contrast pinhole PDI and (b) the ZYGO interferometer [22].

adjustable fringe contrast is easy to realize and high light transmittance (>10%) can be obtained; however, the measurable NA in the fiber method is limited by the NA of the fiber, which is commonly less than 0.2. Besides, the measurable aperture of the test surface is approximately half that of the diffraction wave, both for the pinhole PDI and single-mode fiber PDI shown in **Figure 3**. A PDI system with two optical fibers as point-diffraction sources was developed for full use of the diffracted wavefront [18], in which the diffracted wave from one fiber serves as reference wavefront and that from the other fiber as test wave. Besides, a novel submicron-aperture (SMA) fiber with cone-shaped exit end, as shown in **Figure 4(b)**, has been proposed to obtain both the high diffraction light power and high-NA spherical wavefront [19–21]. The SMA fiber taper surface is coated with metallic film and the exit aperture is formed from the polished tip, it is formed with the same processing technology as manufacturing of fiber-based probes for the scanning near-field optical microscopy. With the SMA fiber, the measurable range can be almost extended to a half space, and the corresponding light transmittance over 50% is obtained [20]. Thus, it is considered as a feasible way to extend the measurement range of the system.

3. PDI for 3D coordinate measurement

In this section, a fiber PDI with submicron aperture [20], which is based on the single-mode fiber with a narrowed exit aperture, for the absolute 3D coordinate measurement within large angle range is described, and the system configuration is shown in **Figure 7**. After passing through the half-wave plate (HWP1), the frequency-stabilized laser beam is separate into p-polarized and s-polarized beams by the polarized beam splitter (PBS), and they are coupled into the single-mode fibers SF1 and SF2, respectively. The exit ends of the fibers SF1 and SF2 are integrated into a target with certain lateral offset, and the output point-diffraction waves W_1 and W_2 interfere on the CCD detector. By translating the PZT scanner, the point-diffraction interference field can be retrieved with phase-shifting method, and the corresponding 3D coordinates of target can be obtained with numerical iterative reconstruction algorithm.

To increase the NA of diffracted wavefront with optical fiber, a single-mode fiber with submicron aperture (as shown in **Figure 4b**) is applied as point-diffraction source. Both the exit ends
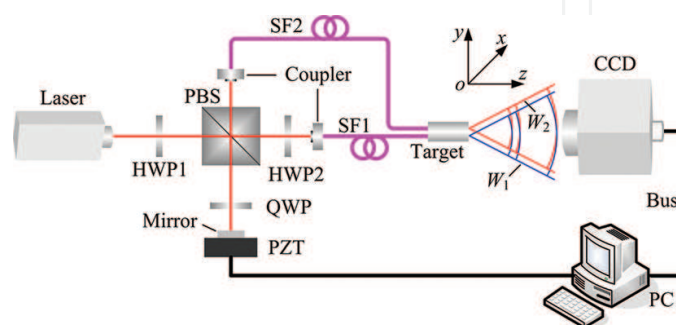

Figure 7. System configuration of the SMA fiber PDI for 3D coordinate measurement [20].

of two single-mode fibers are integrated in a target with certain lateral offset. According to the PDI system shown in **Figure 7**, the absolute 3D coordinates of target can be measured from the phase distribution in interference field corresponding to the optical path difference (OPD), as shown in **Figure 8**.

Denoting the plane of CCD detector as the xy plane and the central position o, with the distances r_1 and r_2 between an arbitrary point $P(x,y,z)$ on the CCD detector and the exit apertures of two fibers on the target, as shown in **Figure 8**, we have the phase difference $\varphi(x,y,z)$,

$$\varphi(x,y,z) = k[r_1(x_1,y_1,z_1;x,y,z)-r_2(x_2,y_2,z_2;x,y,z)], \tag{1}$$

where $k = 2\pi/\lambda$, (x,y,z) is the known 3D coordinate of the point P, (x_1,y_1,z_1) and (x_2,y_2,z_2) are those of two fiber apertures in the target under measurement. According to the one-to-one correspondence relationship of the phase φ at position P (that is the i_{th} pixel on CCD) and 3D coordinates of two fiber apertures in the target, the phase difference can be written as follows:

$$f_i(\mathbf{\Phi}) = k(\varphi^i-\varphi^0)-\widehat{\xi}_i, \tag{2}$$

where the vector $\mathbf{\Phi}$ indicates the coordinates of two fiber apertures under measurement that is $\mathbf{\Phi} =\{(x_1,y_1,z_1);(x_2,y_2,z_2)\}$; $\widehat{\xi}_i$ is the measured phase difference. The phase differences φ^i and φ^0 can be written as follows:

$$\begin{cases} \varphi^i(x^i,y^i,z^i) = k[r_1(x_1,y_1,z_1;x^i,y^i,z^i)-r_2(x_2,y_2,z_2;x^i,y^i,z^i)], \\ \varphi^0(x^0,y^0,z^0) = k[r_1(x_1,y_1,z_1;x^0,y^0,z^0)-r_2(x_2,y_2,z_2;x^0,y^0,z^0)], \end{cases} \tag{3}$$

where (x^i,y^i,z^i) is the 3D coordinate of the i_{th} pixel on CCD. From Eq. (2), various equations can be established corresponding to the pixel positions on the CCD, and we have the matrix equations,
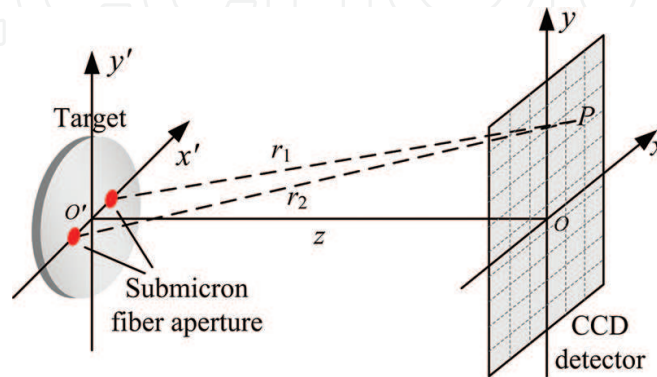

Figure 8. Model for 3D coordinate reconstruction [20].

$$f(\mathbf{\Phi}) = \{f_i(\mathbf{\Phi})\}=\begin{cases} k(\varphi^1-\varphi^0)-\widehat{\xi}_1 \\ \vdots \\ k(\varphi^i-\varphi^0)-\widehat{\xi}_i \\ \vdots \\ k(\varphi^m-\varphi^0)-\widehat{\xi}_m \end{cases}, \qquad (4)$$

where the subscript m is the number of the pixels selected for coordinate reconstruction. For the 6 unknowns in Eq. (2), at least 6 pixels are needed to obtain the 3D coordinates of two fiber apertures. To realize the accurate measurement of 3D coordinates with the PDI system, over 6 pixels could be applied to reconstruct the 3D coordinates, and a quadratic function corresponding to Eq. (4) can be obtained as:

$$F(\mathbf{\Phi}) = \frac{1}{2}f(\mathbf{\Phi})^T f(\mathbf{\Phi}) = \frac{1}{2}\sum_{i=1}^{m}f_i^2(\mathbf{\Phi}). \qquad (5)$$

Thus, the space coordinates of two fiber apertures can be determined from the global minimum $\mathbf{\Phi}^*$ of the function F (that is the least-square solution of Eq. (4)), with a single true solution set.

An experimental SMA-fiber PDI system with aperture size about 0.5 μm, has been set up for the measurement of 3D coordinates. For comparison, the target is installed on the probe of a CMM with the positioning accuracy about 1.0 μm, and the 3D coordinates measured with CMM is taken as the nominal value. **Figure 9** shows the measurement results about the 3D coordinate deviations in x and z directions corresponding to the initial target position (−0.375, 15, and 200) mm. According to **Figure 9**, a good agreement between the CMM results and those from the SMA-fiber PDI system is achieved, and the coordinate measurement errors in x and z directions are 0.47 μm and 0.68 μm RMS, respectively. Due to the decreasing in the light intensity and enlargement in fringe spacing, the measurement error also grows with the increase of measurement distance. Several hardware factors can limit the measurement range
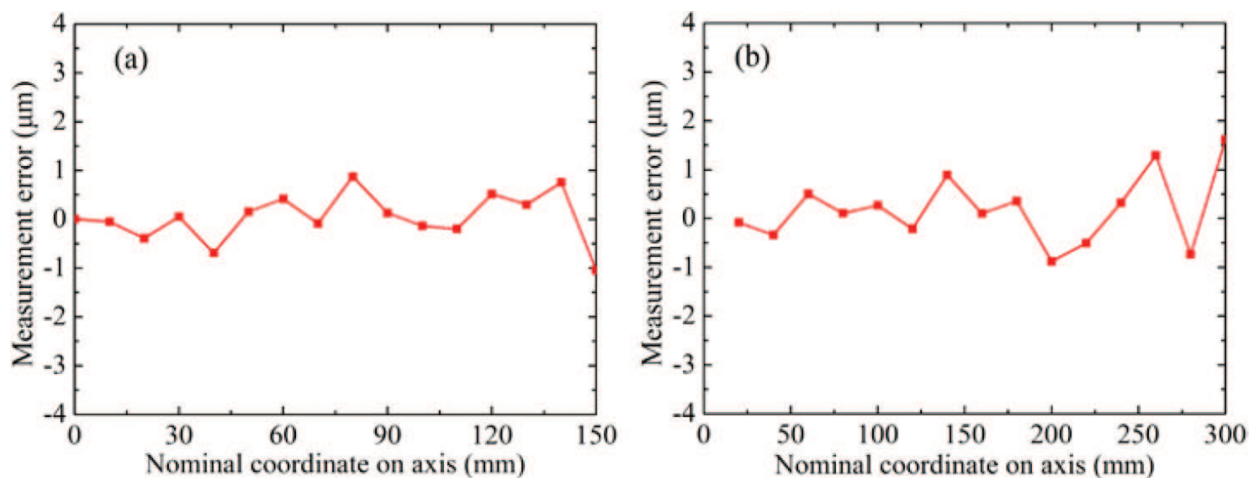

Figure 9. Measurement error in 3D coordinate measurement experiment. Measurement errors in (a) x direction and (b) z direction.

of the PDI system in practical application, including the detector size and light power, though there is no theoretical limit in principle. The PDI system can be further improved by increasing CCD detector size, lateral off set of two SMA fibers and source power. Compared to the traditional single-mode fiber, the SMA fiber provides a feasible way to obtain the ideal spherical reference wavefront, whose aperture angle almost covers half space, and the lateral measurement range is greatly extended.

4. Numerical analysis of point-diffraction wavefront

As one of the most important elements in the PDI, the point source for the diffracted reference wavefront determines the achievable accuracy in the measurement. Purely empirical design of point source parameters is both time consuming and costly. The numerical method based on diffraction theory is a feasible way for the analyzing point-diffraction wavefront. The scalar diffraction theory is valid only when the pinhole size is several times larger than the operating wavelength. For the high-NA spherical wavefront emerging from a tiny aperture with the size comparable with or less than operating wavelength, the vector diffraction theory (that is a nonapproximate method) is required to realize the accurate estimation of diffracted wavefront error. In this section, numerical analysis based on finite difference time domain (FDTD) method (that is a vector diffraction theory) [27] is presented. **Figure 10** shows the flow diagram for the simulation of point-diffraction wavefront based on FDTD method. Due to limitations of computer memory capacity and runtime, FDTD cannot be directly applied to calculate the far-field distribution of pinhole diffraction. In the first step, the near-field distribution of point diffraction is analyzed with the FDTD method, and then the near-to-far field transition based on Huygens' principle is performed to obtain the far-field distribution of point-diffraction wavefront at the position under study. Finally, the sphericity evaluation is carried out to get the departure of point-diffraction wavefront from an ideal sphere.

4.1. Simulation of pinhole diffraction

Figure 11 shows the amplitude and phase distribution in the near-field diffraction, respectively, corresponding to the pinholes of 0.5 μm and 1 μm diameters, respectively. According to **Figure 11**, the phase distribution within Airy disk range is close to an ideal sphere, and the angle of Airy disk increases with the decrease of pinhole diameter.
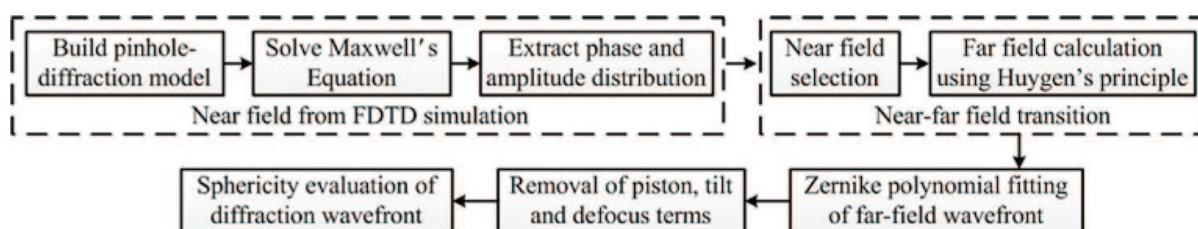

Figure 10. Procedure for simulation of point-diffraction wavefront based on FDTD method.
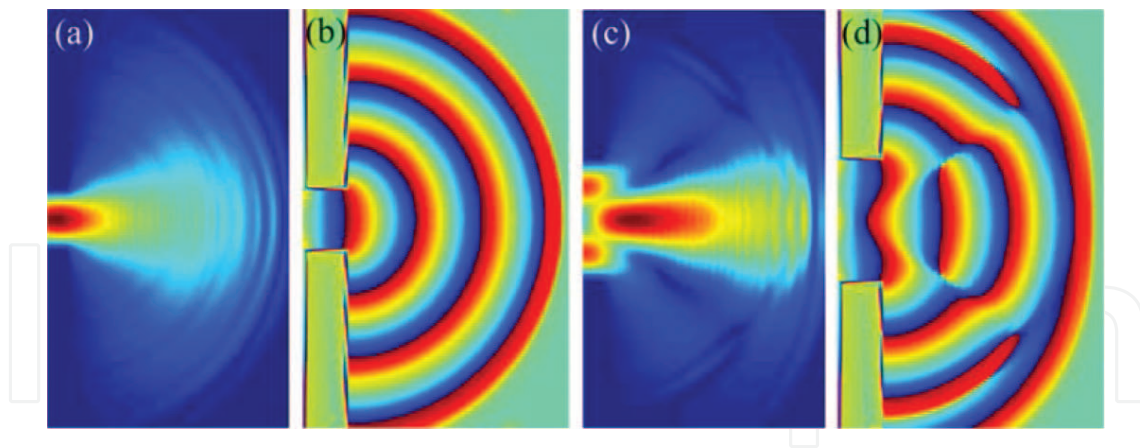
Figure 11. Near-field distribution of pinhole-diffraction wavefront. (a) Amplitude and (b) phase distribution with 0.5 μm-diameter pinhole; (c) amplitude and (d) phase distribution with 1 μm-diameter pinhole [27].
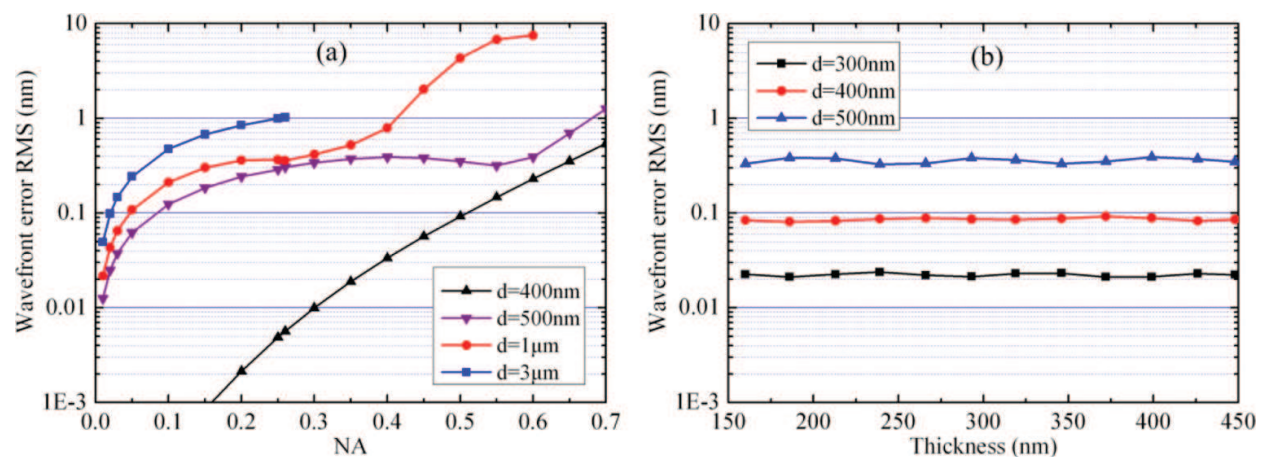

Figure 12. Simulation results for pinhole-diffraction wavefront. (a) Diffracted wavefront error over various NAs for different pinhole diameters, and (b) diffracted wavefront error under various film thicknesses [27].

To analyze the wavefront error where the test surface with 500 mm curvature radius is placed, far field is positioned at 500 mm away from pinhole. The wavefront errors over various NAs of diffracted wavefronts corresponding to different pinhole diameters are shown in **Figure 12(a)**. According to **Figure 12(a)**, the point-diffraction wavefront error grows both with the pinhole size and NA range, and the wavefront error RMS for the 1 μm pinhole diameter over 0.35 NA is smaller than 0.53 nm. Thus, it can be taken as ideal reference wavefront and applied to realize the measurement accuracy reaching to RMS $\lambda/1000$ (λ = 532 nm). Besides, larger diffraction angle could be obtained with smaller pinhole, and it allows much higher measurable NA. The diffraction angle corresponding to 1 μm pinhole diameter is about 75°, and that for 3 μm pinhole diameter is about 30°. Thus, the small pinhole is required in the testing of surfaces with high NA. However, the small pinhole size would result in significant reduction of diffraction light intensity. The pinhole size could be optimized according to the requirement of testing accuracy and achievable diffracted wavefront precision corresponding to various pinhole diameters. The pinhole in PDI plays not only the role as a filter to remove the

aberration in diffracted wavefront, but also as waveguide. **Figure 12(b)** shows the numerical results about the effect of film thickness on diffracted wavefront for different pinhole diameters, with the thickness ranging from 150 nm to 450 nm. The mean values of wavefront error RMS corresponding to 300 nm, 400 nm, and 500 nm pinhole diameters are about 0.02 nm, 0.08 nm, and 0.36 nm, respectively, and the corresponding fluctuation ranges are within 10%. Thus, the effect of variation in film thickness ranging from 150 nm to 450 nm is negligible.

4.2. Simulation of SMA fiber diffraction

Figure 13(a) shows the simulation results about the full wavefront aperture angle for the SMA fibers with various exit apertures [20]. According to **Figure 13(a)**, the full aperture angle of diffracted wave obviously increases with the decreasing of fiber aperture, and that corresponding to the 0.5 μm fiber aperture are about 160°, providing the necessary conic boundary to extend the measurement range almost within a half space. **Figure 13(b)** shows the wavefront errors over various NAs of diffracted wavefronts corresponding to different SMA fiber apertures [20]. From **Figure 13(b)**, the increase in NA range and fiber aperture could lead to the growth of diffracted wavefront error. The wavefront error over 0.70 NA range for the 0.5 μm fiber aperture is better than $\lambda/1000$ RMS, and it can be applied as ideal spherical reference wave in the PDI system.

Figure 14 shows the analyzing result about light transmittance in the point diffraction both with the SMA fiber method and pinhole method. According to **Figure 14**, the light transmittance in both the SMA fiber diffraction and pinhole diffraction grows with the increase in aperture size. It can be seen from **Figures 12(a)** and **13(a)** that the similar aperture angles can be obtained with the same diffraction aperture size, however, the light transmittance in the SMA fiber diffraction is far larger than that in pinhole diffraction according to **Figure 14**. The light transmittance corresponding to the 0.5 μm aperture in the SMA fiber method and pinhole method is about 67% and 6%, respectively. Thus, the SMA fiber provides a feasible way to
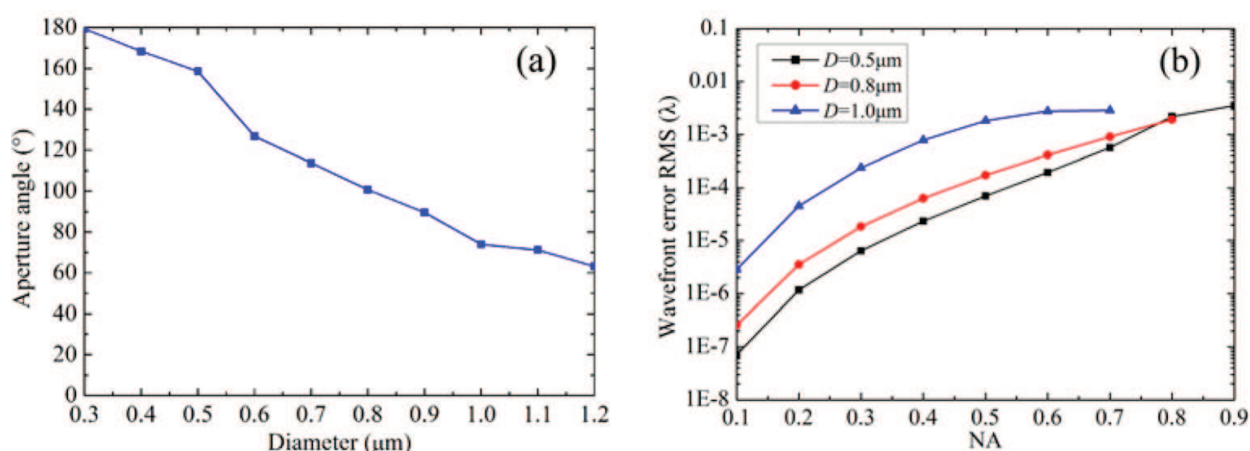

Figure 13. Simulation results for SMA-fiber-diffraction wavefront. (a) Aperture angle of diffracted wave and light transmittance for various fiber apertures, and (b) diffracted wavefront error within various NA ranges for different fiber apertures [20].
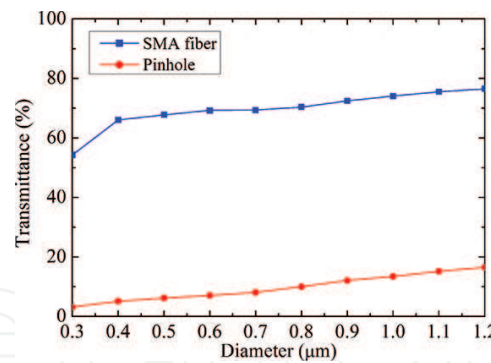
Figure 14. Simulation results for the light transmittance in pinhole diffraction and SMA fiber diffraction.

obtain the high light intensity required in the optical testing, enabling the extension of measurement range with PDI system.

5. Experimental measurement of point-diffraction wavefront

The numerical simulation based on the vector diffraction theory such as FDTD method provides an easy and efficient way to estimate the point-diffraction wavefront error. However, both the computational accuracy and complex practical factors (such as environmental disturbance and performances of various optical parts) can introduce significant deviation from an ideal case. Due to the accuracy limitation of standard optics, the traditional interferometers fail to measure the point-diffraction wavefront error, which is expected to be in the order of subnanometer or even smaller. Various experimental testing methods have been proposed to measure the point-diffraction wavefront error, the majority of which are based on the hybrid method [15] and null test [28]. Typically, the hybrid method requires several measurements with the rotation and displacement of the optics under test, it is sensitive to environmental disturbance and cannot completely separate the systematic error. The null test is a self-reference method, and it is widely applied to reconstruct the point-diffraction wavefront and calibrate the PDI. However, it requires the foreknowledge about the system configuration to remove the high-order aberrations, which are introduced by the point-source separation and cannot be negligible in the case of high-NA wavefront. In this section, a high-precision measurement method, which is based on shearing interferometry, is presented to analyze the point-diffraction wavefront from SMA fiber [21].

Figure 15 shows the schematic diagram of SMA fiber projector used to evaluate the sphericity of point-diffraction wavefront. The SMA fiber can be applied to obtain both high diffraction light power and high-NA spherical wavefront. Four parallel SMA single-mode fibers S_1, S_2, S_3, and S_4 with coplanar exit ends are integrated in a metal tube. To obtain the identical wavefront parameters, the four SMA fibers with same aperture size and cone angle are carefully chosen in the experiment to minimize the measurement error. The coherent beams are coupled into the SMA fibers, and the point-diffraction waves from the fibers interfere on a detection plane, as shown in **Figure 15(b)**. By alternatively switching on the waves from the fiber pairs G_1 (S_1 and S_2) and G_2
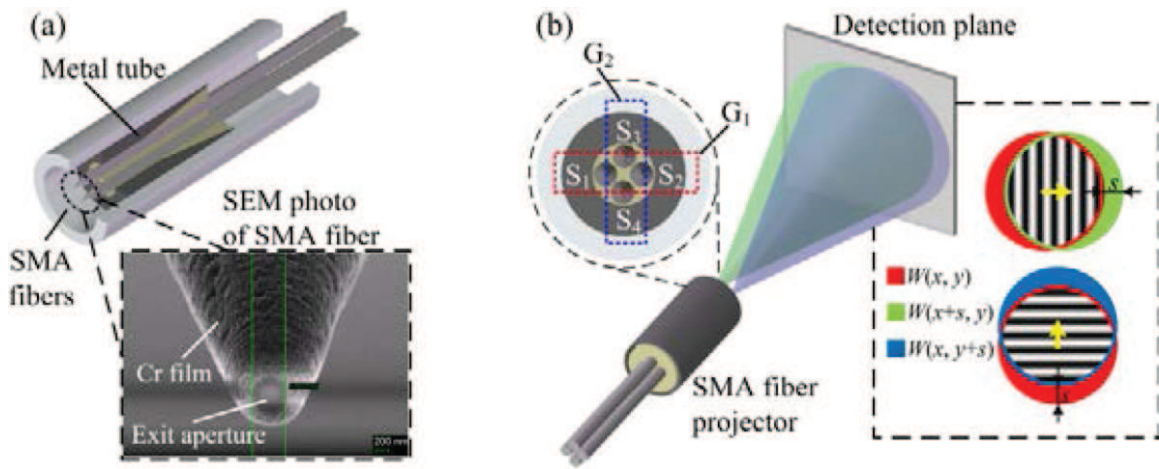
Figure 15. Schematic diagram of SMA fiber point-diffraction wavefront measurement system. (a) Structure of SMA fiber projector and (b) schematic diagram of SMA fiber point-diffraction wavefront measurement [21].

(S_3 and S_4), the shearing interferograms in x and y directions can be obtained and the corresponding shearing wavefronts can be measured with a phase-shifting method, respectively.

5.1. Point-diffraction wavefront retrieval method

With the shearing wavefronts obtained from the projector shown in **Figure 15**, the differential Zernike polynomials fitting method can be applied to retrieve the SMA fiber point-diffraction wavefront. Denoting the point-diffraction wavefront under test as $W(x, y)$, we have the shearing wavefronts $\Delta W_x(x, y)$ and $\Delta W_y(x, y)$ in x and y directions,

$$\begin{cases} \Delta W_x(x,y) = W(x,y) - W(x + s, y) \\ \Delta W_y(x,y) = W(x,y) - W(x, y + s) \end{cases}, \tag{6}$$

where s is the shearing amount as shown in **Figure 15(b)**. The wavefront $W(x, y)$ can be described with Zernike polynomials and can be decomposed into a series (N terms) of orthonormal polynomials $\{Z_i(x, y)\}$ with the corresponding coefficients $\{a_i\}$,

$$W(x,y) = \sum_{i=1}^{N} a_i Z_i(x,y). \tag{7}$$

According to Eqs. (6) and (7), the shearing wavefronts $\Delta W_x(x, y)$ and $\Delta W_y(x, y)$ can be expressed as follows:

$$\begin{cases} \Delta W_x(x,y) = \sum_{i=1}^{N} a_i \Delta Z_{i,x}(x,y) \\ \Delta W_y(x,y) = \sum_{i=1}^{N} a_i \Delta Z_{i,y}(x,y) \end{cases}, \tag{8}$$

where the differential Zernike polynomials $\Delta Z_{i,x}(x, y)$ and $\Delta Z_{i,y}(x, y)$ can be written as follows:

$$\begin{cases} \Delta Z_{i,x}(x,y) = Z_i(x,y) - Z_i(x+s,y) \\ \Delta Z_{i,y}(x,y) = Z_i(x,y) - Z_i(x,y+s) \end{cases}. \tag{9}$$

Denoting the shearing wavefronts, differential Zernike polynomials and the coefficients in Eq. (8) as $\Delta \mathbf{W} = (\Delta W_x, \Delta W_y)^T$, $\Delta \mathbf{Z} = (\Delta Z_{i,x}, \Delta Z_{i,y})^T$ and $\mathbf{a}$, respectively, Eq. (8) can be transformed into a matrix form,

$$\Delta \mathbf{W} = \Delta \mathbf{Z} \mathbf{a}. \tag{10}$$

Thus, the coefficients $\{a_i\}$ of Zernike polynomials in Eq. (7) can be obtained from the least-squares solution of Eq. (10),

$$\mathbf{a} = (\Delta \mathbf{Z}^T \Delta \mathbf{Z})^{-1} \Delta \mathbf{Z}^T \Delta \mathbf{W}. \tag{11}$$

According to Eq. (11), the retrieval of point-diffraction wavefront $W(x,y)$ depends on the measurement precision of shearing wavefronts $\Delta W_x(x,y)$ and $\Delta W_y(x,y)$. Traditionally, the systematic error introduced by lateral displacement between SMA fibers can be calibrated by removing Zernike tilt and power terms. However, the residual high-order aberrations can significantly influence the measurement precision, especially in the case of high NA and large lateral displacement. Thus, a general and rigorous method for geometric error removal is required to realize the high-precision measurement of point-diffraction wavefront.

5.2. High-precision method for systematic error calibration

In the null test of pinhole diffraction wavefront and single-mode fiber diffraction wavefront, the high wavefront NA in a pinhole PDI and large lateral displacement between fibers in fiber PDI could introduce some high-order geometric aberrations, respectively. Different from traditional pinhole PDI and single-mode fiber PDI, the null test of SMA fiber diffraction wavefront involves both high NA and large lateral displacement, placing much higher requirement on the calibration of the systematic error introduced by lateral displacement between SMA fibers. A double-step calibration method based on three-dimensional coordinate reconstruction and symmetric lateral displacement compensation can be applied to completely remove systematic error. It should be noted that the possible longitudinal displacement between SMA fibers may also introduce certain systematic error; however, it can be well minimized with the fine adjusting mechanism. Besides, the error introduced by the longitudinal displacement is low-order aberration, and it can be well calibrated with traditional misalignment calibration method by subtracting the Zernike piston, tilt and power terms.

5.2.1. First-step calibration based on three-dimensional coordinate reconstruction

Without loss of generality, we take the displacement in x direction between SMA fibers as the geometric error calibration model to be analyzed, as shown in **Figure 16**.

Supposing that the distance between exit apertures of fiber pairs G_1 (S_1 and S_2) and an arbitrary point $P(x,y,z)$ on the detection plane are R_1 and R_2, we have the corresponding optical path difference OPD,

$$\mathrm{OPD} = R_1(x_1, y_1, z_1; x, y, z) - R_2(x_2, y_2, z_2; x, y, z), \tag{12}$$

where (x_1, y_1, z_1) and (x_2, y_2, z_2) are the three-dimensional coordinates of S_1 and S_2, (x, y, z) is that of the arbitrary known point P. To simplify the analysis, the origin of the coordinate system is located at S_1, the distance between the SMA fiber projector and CCD detector is D. Thus, the OPD in Eq. (12) can be simplified as follows:

$$\mathrm{OPD} = \sqrt{x^2 + y^2 + D^2} - \sqrt{(x+s)^2 + y^2 + D^2}. \tag{13}$$

According to the one-to-one correspondence of the OPD distribution on the detection plane and the coordinate of fiber apertures, the 3D coordinate measurement method with PDI introduced in Section 3 can be applied to reconstruct the 3D coordinates in Eq. (12) that is the global minimum $\boldsymbol{\Phi}^*$ of the residual function $F(\boldsymbol{\Phi})$,

$$F(\boldsymbol{\Phi}) = \sum_k f_k^2(\boldsymbol{\Phi}) = \sum_k (\mathrm{OPD}_k - \widehat{\xi}_k)^2, \tag{14}$$

where the vector $\boldsymbol{\Phi} = \{(x_1, y_1, z_1); (x_2, y_2, z_2)\}$ is the coordinates of SMA fibers under measurement, the subscript k indicates the point number on the detection plane, $\widehat{\xi}_k$ is the measured OPD and OPD_k is the OPD reconstructed from coordinates $\boldsymbol{\Phi}$ according to Eq. (13). With the reconstructed coordinates $\boldsymbol{\Phi}^*$, the systematic error can be preliminarily calibrated,

$$\mathrm{OPD}_1 = \mathrm{OPD}(\boldsymbol{\Phi}) - \mathrm{OPD}(\boldsymbol{\Phi}^*). \tag{15}$$

However, the reconstruction accuracy of fiber coordinates can only reach the order of submicron in the practical case, resulting in obvious residual error in the calibration result. The root mean square (RMS) value of the residual error in the preliminary calibration is 0.0077λ corresponding to the 0.5 μm coordinate reconstruction error for 0.60 NA fibers and 250 μm lateral displacement between two fibers. To further remove the residual systematic error, a second-step calibration, which is based on symmetric lateral displacement compensation, needs to be carried out.
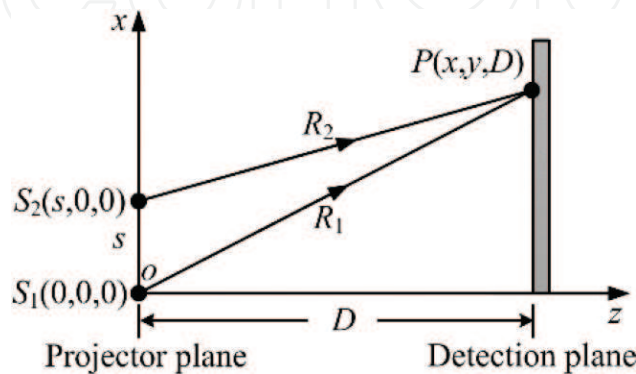

Figure 16. Geometry for systematic error analysis [21].

5.2.2. Second-step calibration based on symmetric lateral displacement compensation

The expression for OPD in Eq. (12) can be simplified as follows:

$$\text{OPD} \cong a_2 Z_2 + a_9 Z_9 + a_{19} Z_{19} + a_{33} Z_{33}, \tag{16}$$

where Z_2 refers to x tilt terms, Z_9, Z_{19}, and Z_{33} are Zernike primary, secondary, and tertiary x coma terms, respectively, a_2, a_9, a_{19}, and a_{33} are the corresponding coefficients, and

$$\begin{cases} a_2 = s[-t - ts^2/(2D^2) + t^3/3 + 3t^3 s^2/(4D^2) - 3t^5/16 - 15t^5 s^2/(16D^2) + t^7/8] \\ a_9 = s[t^3/6 + 3t^3 s^2/(8D^2) - 3t^5/20 - 15t^5 s^2/(20D^2) + t^7/8] \\ a_{19} = s[-3t^5/80 - 3t^5 s^2/(16D^2) + 3t^7/56] \\ a_{33} = s(t^7/112) \end{cases} \tag{17}$$

Similarly, the reconstructed optical path difference $\text{OPD}(\Phi^*)$ (though with certain coordinate reconstruction error) follows the relationship given by Eq. (16). Thus, the residual systematic error OPD_1 after first-step calibration, according to Eqs. (15) and (16), can be written as follows:

$$\text{OPD}_1 \cong \Delta a_2 Z_2 + \Delta a_9 Z_9 + \Delta a_{19} Z_{19} + \Delta a_{33} Z_{33}, \tag{18}$$

where $\{\Delta a_i\}$ (i = 2, 9, 19, 33) are the corresponding Zernike coefficients. With the implementation of the first-step calibration, the coordinate reconstruction error reaches the order of submicron, and the corresponding approximation error in Eq. (18) can be well restricted and is negligible. According to Eq. (16), the major systematic error introduced by the lateral displacement includes tilt and coma terms, they cannot be completely removed with traditional misalignment calibration method by subtracting the Zernike piston, tilt and power terms. From Eq. (16), the residual coma aberration due to lateral displacement depends on the lateral displacement s, NA, and distance D, the corresponding Zernike coefficients are odd functions about s. Thus, the superposition of geometric errors $\text{OPD}^{(s)}$ and $\text{OPD}^{(-s)}$ corresponding to opposite shear directions can be expressed as follows:

$$\text{OPD}^{(s)} + \text{OPD}^{(-s)} \cong 0. \tag{19}$$

According to the analysis above, the geometric error can be further reduced by superposing two measurements with opposite shear directions, corresponding to lateral displacement s and $-s$, respectively. Denoting the preliminarily calibrated wavefront data corresponding to lateral displacement s and $-s$ as $W_{m1}^{(s)}$ and $W_{m1}^{(-s)}$, and the true shearing wavefront under test ΔW, we have

$$\begin{cases} W_{m1}^{(s)} = \Delta W + \text{OPD}_1^{(s)} \\ W_{m1}^{(-s)} = \Delta W + \text{OPD}_1^{(-s)} \end{cases} \tag{20}$$

According to Eqs. (19) and (20), the shearing wavefront ΔW can be obtained with

$$\Delta W \cong (W_{m1}^{(s)} + W_{m1}^{(-s)})/2. \tag{21}$$

To get the measurement data with the lateral displacement −s, one may rotate the SMA fiber projector by 180°. **Figure 17(a)** and **(b)** shows the residual systematic errors corresponding to various lateral displacement amounts with different NAs with traditional method and the double-step calibration method. The traditional method is not valid when the lateral displacement is over 50 μm because the residual error RMS is larger than $2.0 \times 10^{-3}\lambda$ with the 0.10 NA fiber. The residual error also increases significantly with the lateral displacement, especially for the case with high NA fiber. In **Figure 17(b)**, the residual error is less than $1.0 \times 10^{-4}\lambda$ RMS within a 300 μm lateral displacement even for the 0.60 NA fiber, it confirms the feasibility of the double-step calibration in Section 5.2.

To obtain point-diffraction spherical wavefront in the experiment, the projector should be placed at the far-field zone that is the distance $D >> 2(2d)^2/\lambda$ from the fibers [29], where d is the aperture size. With the unwrapped phase distribution, the systematic error calibration is carried out to obtain the shearing wavefront with the high-precision double-step calibration method introduced in Section 5.2. The experimental measurement of SMA fiber point-diffraction wavefront has been carried out with the system diagram shown in **Figure 15**. The unwrapped original wavefront before and after 180° rotation in x and y directions is shown in **Figure 18(a)–(d)**, and the corresponding precalibrated shearing wavefronts after the first-step calibration are shown in **Figure 18(f)–(i)**, respectively. **Figure 18(e)** and **(j)** is the true shearing wavefronts in x and y directions obtained with the double-step calibration method. According to **Figure 18**, obvious residual errors can be seen in the obtained wavefronts after first-step calibration, the precalibrated shearing wavefront error RMS in x and y directions are 0.0254λ and 0.0194λ, respectively. The residual error is further removed after the second-step calibration, and true shearing wavefront error RMS in x and y directions are $1.38 \times 10^{-4}\lambda$ and $1.36 \times 10^{-4}\lambda$, respectively. Besides, there is no significant odd error in the finally retrieved wavefronts in **Figure 18(e)** and **(j)**. Thus, the high-accuracy calibration is realized with the proposed method.
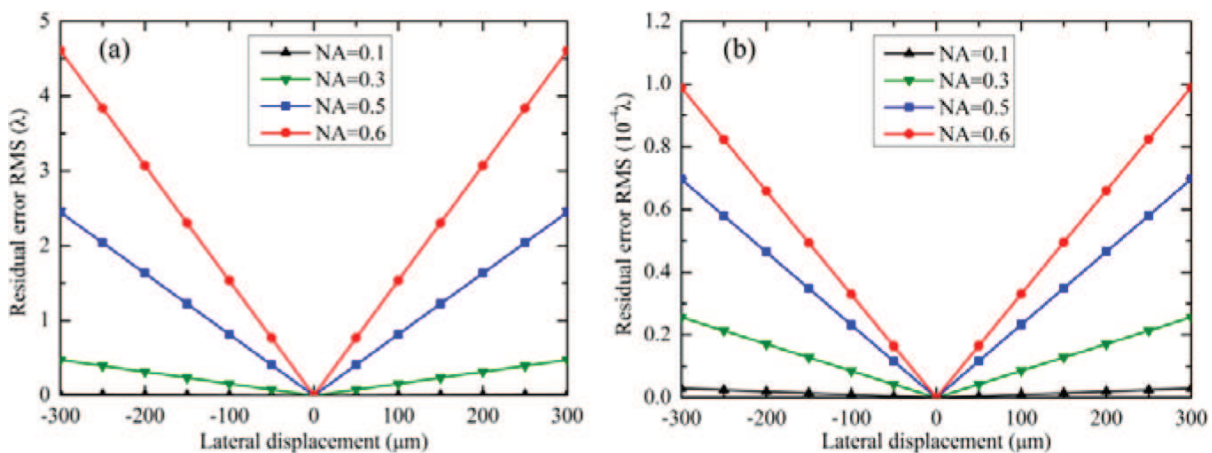

Figure 17. Residual errors in the calibration of systematic error under various lateral displacements and NAs in computer simulation. (a) RMS value with traditional method and (b) RMS value with the proposed double-step calibration method [21].

With the true shearing wavefronts in x and y directions after systematic error calibration, the point-diffraction wavefront can be reconstructed based on the differential Zernike polynomials fitting method introduced in Section 5.1. The measured wavefront error compared with an ideal sphere is shown in **Figure 19(a)**, PV and RMS are $9.20 \times 10^{-4}\lambda$ and $1.54 \times 10^{-4}\lambda$, respectively. **Figure 19(b)** and **(c)** shows the measured wavefronts after the 45° rotation and translation along z direction of projector, respectively. It can be seen from **Figure 19** that the measured wavefront shape in the original position agrees well with those obtained with projector rotation and translation, demonstrating the measurement repeatability and accuracy. The protective glass on CCD detector could introduce additional deformation on point-diffraction wavefront, and the measurement accuracy is expected to be further improved by removing the protective glass. Due to the smoothing effect of each pixel, the relatively large pixel acts as a low-pass filter and the measured wavefront should be taken as a macroparameter. By adopting
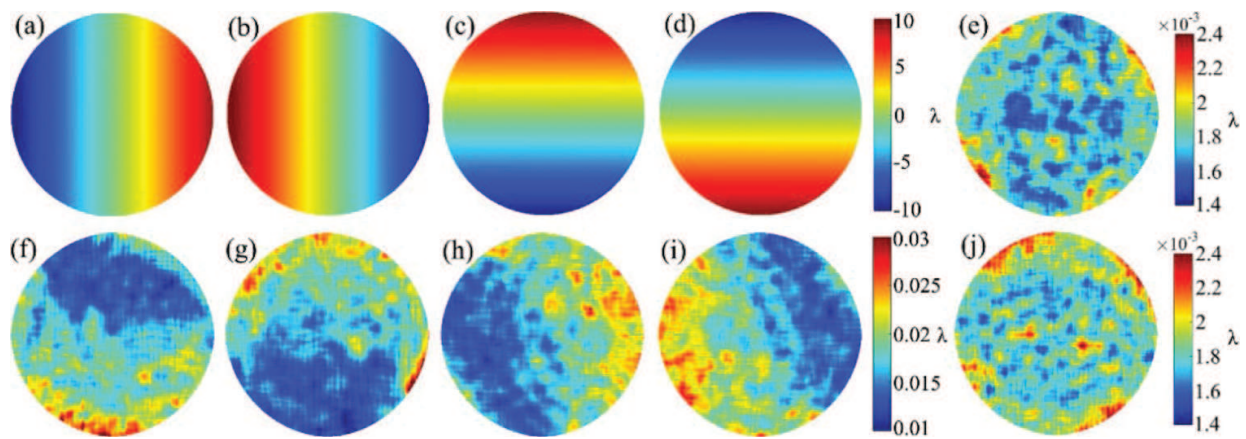

Figure 18. Measurement results of shearing wavefront retrieval in SMA fiber point-diffraction wavefront measurement. Unwrapped original wavefronts, including (a) x direction and (c) y direction before 180° rotation, (b) x direction and (d) y direction after 180-degree rotation; shearing wavefronts after the first-step calibration, including (f) x direction and (h) y direction before 180° rotation, (g) x direction and (i) y direction after 180-degree rotation; finally retrieved shearing wavefronts after the double-step calibration, including (e) x and (j) y directions [21].
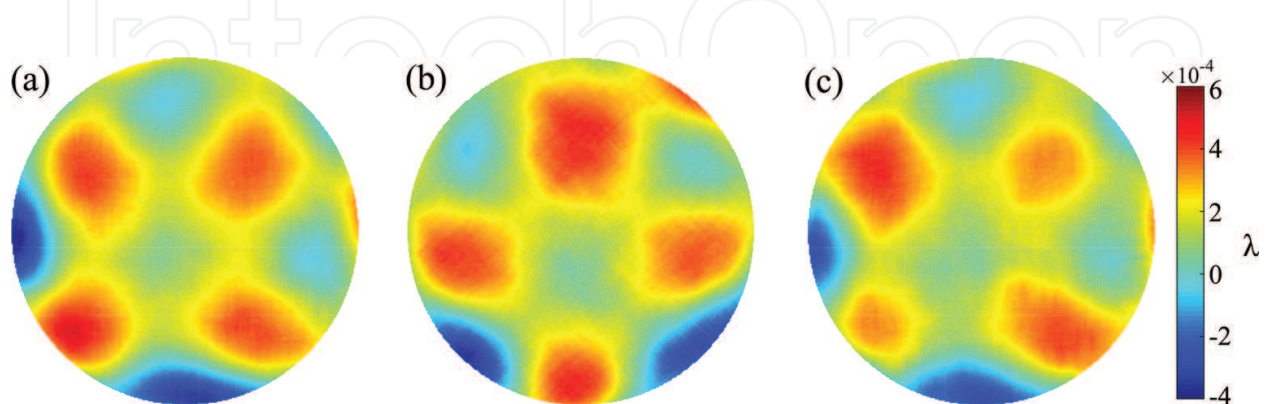

Figure 19. Experimental result of point-diffraction wavefront measurement. (a) Measured point-diffraction wavefront in original position, (b) measured wavefront after 45° projector rotation, and (c) measured wavefront after projector translation [21].

the CCD with smaller pixel size and placing the SMA fiber projector at a position farther from CCD detector, the smoothing effect can be further decreased.

6. Conclusion

In this chapter, the application of PDI system in the wavefront and surface testing is introduced. Various PDI setups, including the fiber PDI and pinhole PDI, have developed for high-accuracy optical testing, and the measurement accuracy up to subnanometer was reported. Different from the pinhole PDI, the adjustable fringe contrast is easily realized with fiber PDI, and it can be applied to test the surface with various reflectivities. To realize the adjustable fringe contrast with pinhole method, the polarizing elements with special structure is needed to transform the polarization states and adjust the relative intensities of the interfering testing and reference beams. High measurable NA can be achieved with the pinhole; however, the light transmission is quite low; high light transmittance can be obtained with single-mode fiber; however, the measurable NA is limited by the NA of the fiber. To obtain both the high diffraction light power and high-NA spherical wavefront, a SMA fiber with cone-shaped exit end has been proposed, and it is considered as a feasible way to extend the measurement range of the system. Based on the SMA fiber, a PDI system for the absolute 3D coordinate measurement was proposed. The system utilizes the SMA fiber to get spherical wave with both high NA and high light intensity, and large measurable range is achieved.

The numerical study of point-diffraction wavefront both with pinhole and SMA fiber is performed, which is based on the FDTD method. The aperture angle, light transmittance, and wavefront error are analyzed. According to simulation results, the ideal spherical wavefront with the accuracy better than subnanometer can be obtained both with pinhole and SMA fiber, and the increase in NA range and diffraction aperture size could lead to the growth of diffracted wavefront error. It can be seen from the comparison of pinhole diffraction and SMA fiber diffraction, the light transmittance in both the methods grows with the increase in aperture size, and the similar aperture angles can be obtained with the same diffraction aperture size. However, the light transmittance in SMA fiber diffraction is far larger than that in pinhole diffraction. Thus, the SMA fiber provides a feasible way to obtain the high light intensity required in the optical testing, enabling the extension of measurement range with PDI system.

The experimental measurement of SMA fiber point-diffraction wavefront is carried out to evaluate its accuracy in practical application, which is based on shearing interferometry. To realize the high-precision calibration of the systematic error introduced by the lateral displacement between SMA fibers, a double-step calibration method based on three-dimensional coordinate reconstruction and symmetric lateral displacement compensation is used to remove the geometric aberration from the shearing wavefront. Besides, the differential Zernike polynomials fitting method is used to reconstruct the point-diffraction wavefront. The spherical wavefront with the accuracy reaching the order of $10^{-4}\lambda$ is obtained in the experiment. The calibration method can be performed without any preknowledge about the measurement system configuration. It realizes the high-accuracy measurement of point-diffraction wavefront and also provides a feasible method for geometric aberration calibration in interferometric system.

Acknowledgements

Author details

Daodang Wang[1]* and Rongguang Liang[2]

*Address all correspondence to: wangdaodang@sina.com

1 College of Metrology and Measurement Engineering, China Jiliang University, Hangzhou, China

2 College of Optical Sciences, University of Arizona, Tucson, AZ, USA

References

[1] Stulen R H, Sweeney D W. Extreme ultraviolet lithography. IEEE Journal of Quantum Electronics. 1999; **35**(5): 694–699. DOI: 10.1109/3.760315

[2] Goldberg K A, Naulleau P P, Denham P E, Rekawa S B, Jackson K, Anderson E H, et al. At-wavelength alignment and testing of the 0.3 NA MET optic. Journal of Vacuum Science & Technology B. 2004; **22**(6): 2956–2961. DOI: 10.1116/1.1815303

[3] Otaki K, Zhu Y, Ishii M, Nakayama S, Murakami K, Gemma T. Rigorous wavefront analysis of the visible-light point diffraction interferometer for EUVL. Proceeding of SPIE. 2004; **5193**: 182–190. DOI: 10.1117/12.507046

[4] Takeuchi S, Kakuchi O, Yamazoe K, Gomei Y, Decker T A, Johnson M A, et al. Visible light point-diffraction interferometer for testing of EUVL optics. Proceeding of SPIE. 2006; **6151**: 61510E. DOI: 10.1117/12.656275

[5] Malacara D. Twyman-Green Interferometer. In: Malacara D, editor. Optical Shop Testing. 3rd ed. New Jersey: Wiley; 2007. pp. 46–96.

[6] Mantravadi M V, Malacara D. Newton, Fizeau, and Haidinger interferometers. In: Malacara D, editor. Optical Shop Testing. 3rd ed. New Jersey: Wiley; 2007. pp. 1–45.

[7] Smartt R N, Steel W H. Theory and application of point-diffraction interferometers. Japanese Journal of Applied Physics. 1975; **14**(S1): 351–356. DOI: 10.7567/JJAPS.14S1.351

[8] Wang G Y, Zheng Y L, Sun A M, Wu S D, Wang Z J. Polarization pinhole interferometer. Optics Letters. 1991; **16**(17): 1352–1354. DOI: 10.1364/OL.16.001352

[9]   Gong Q, Geary J M. Modeling point diffraction interferometers. Optical Engineering. 1996; **35**(2): 351–356. DOI: 10.1117/1.600903

[10] Millerd J E, Martinek S J, Brock N J, Hayes J B, Wyant J C. Instantaneous phase-shift, point-diffraction interferometer. Proceeding of SPIE. 2004; **5380**: 422–429. DOI: 10.1117/12.557126

[11] Gong Q, Eichhorn W. Alignment and testing of piston and aberrations of a segmented mirror. Proceeding of SPIE. 2005; **5869**: 586912. DOI: 10.1117/12.613657

[12] Neal R M, Wyant J C. Polarization phase-shifting point-diffraction interferometer. Applied Optics. 2006; **45**(15): 3463–3476. DOI: 10.1364/AO.45.003463

[13] Otaki K, Bonneau F, Ichihara Y. Absolute measurement of spherical surface by point diffraction interferometer. Proceeding of SPIE. 1999; **3740**: 602–605. DOI: 10.1117/12.347755

[14] Otaki K, Ota K, Nishiyama I, Yamamoto T, Fukuda Y, Okazaki S. Development of the point diffraction interferometer for extreme ultraviolet lithography: design, fabrication, and evaluation. Journal of Vacuum Science & Technology B. 2002; **20**(6): 2449–2458. DOI: 10.1116/1.1526605

[15] Otaki K, Yamamoto T, Fukuda Y, Ota K, Nishiyama I, Okazaki S. Accuracy evaluation of the point diffraction interferometer for extreme ultraviolet lithography aspheric mirror. Journal of Vacuum Science & Technology B. 2002; **20**(1): 295–300. DOI: 10.1116/1.1445161

[16] Sommargren G E. Phase shifting diffraction interferometry for measuring extreme ultraviolet optics. OSA Trends in Optics & Photonics. 1996; **V4**: 108–112.

[17] Kihm H, Kim S W. Oblique fiber optic diffraction interferometer for testing. Optical Engineering. 2005; **44**(12): 125601. DOI: 10.1117/1.2148367

[18] Matsuura T, Udaka K, Oshikane Y, Inoue H, Nakano M, Yamauchi K, et al. Spherical concave mirror measurement by phase-shifting point diffraction interferometer with two optical fibers. Nuclear Instruments & Methods in Physics Research A. 2010; **616**(2–3): 233–236. DOI: 10.1016/j.nima.2009.12.031

[19] Chkhalo N I, Klimov A Y, Rogov V V, Salashchenko N N, Toropov M N. A source of a reference spherical wave based on a single mode optical fiber with a narrowed exit aperture. Review of Scientific Instruments. 2008; **79**(3): 033107. DOI: 10.1063/1.2900561

[20] Wang D, Chen X, Xu Y, Wang F, Kong M, Zhao J, et al. High-NA fiber point-diffraction interferometer for three-dimensional coordinate measurement. Optics Express. 2014; **22**(21): 25550–25559. DOI: 10.1364/OE.22.025550

[21] Wang D, Xu Y, Liang R, Kong M, Zhao J, Zhang B, et al. High-precision method for submicron-aperture fiber point-diffraction wavefront measurement. Optics Express. 2016; **24**(7): 7079–7090. DOI: 10.1364/OE.24.007079

[22] Rhee H-G, Kim S-W. Absolute distance measurement by two-point-diffraction interferometry. Applied Optics. 2002; **41**(28): 5921–5928. DOI: 10.1364/AO.41.005921

[23] Rhee H-G, Chu J, Lee Y-W. Absolute three-dimensional coordinate measurement by the two-point diffraction interferometry. Optics Express. 2007; **15**(8): 4435–4444. DOI: 10.1364/OE.15.004435

[24] Wang D, Yang Y, Chen C, Zhuo Y. Point diffraction interferometer with adjustable fringe contrast for testing spherical surfaces. Applied Optics. 2011; **50**(16): 2342–2348. DOI: 10.1364/AO.50.002342

[25] Medecki H, Tejnil E, Goldberg K A, Bokor J. Phase-shifting point diffraction interferometer. Optics Letters. 1996; **21**(19): 1526–1528. DOI: 10.1364/OL.21.001526

[26] Johnson M A, Phillion D W, Sommargren G E, Decker T A, Taylor J S, Gomei Y, et al. Construction and testing of wavefront reference sources for interferometry of ultra-precise imaging systems. Proceeding of SPIE. 2005; **5869**: 58690P. DOI: 10.1117/12.623185

[27] Wang D, Wang F, Zou H, Zhang B. Analysis of diffraction wavefront in visible-light point-diffraction interferometer. Applied Optics. 2013; **52**(31): 7602–7608. DOI: 10.1364/AO.52.007602

[28] Naulleau P, Goldberg K, Lee S, Chang C, Bresloff C, Batson P, et al. Characterization of the accuracy of EUV phase-shifting point diffraction interferometry. Proceeding of SPIE. 1998; **3331**: 114–123. DOI: 10.1117/12.309563

[29] Kong J A. Electromagnetic Wave Theory. 1st ed. New Jersey: Wiley; 1986. 667 p.